SUPPLEMENTARY MATERIAL

Supplementary Note 1: Additional ice histories

We construct three additional ice histories that adopt the same GMSL history as ICE-PC2 (as in main text, Figure 2A) but vary the geographic extent of ice. In ICE-PC, ice sheets grow in the same geometry as they decay (that is, as in our modified ICE-5G history, the ice geometry during the glaciation phase is assumed to be identical to the post-LGM geometry when the eustatic sea-level value is the same; Supplementary Figure 1E). In ICE-PC3, the eastern sector of the LIS is ice-free (as in ICE-PC2) from 80-44 ka except for northern Quebec, which remains glaciated, according to retrodicted patterns of snow accumulation (e.g. Löfverström et al. 2014; Supplementary Figure 1F). Lastly, ICE-PC4 has the same ice extent as ICE-PC2 at 44 ka, but the ice configuration at the LGM is modified to match the moraine limits in Braun (2004) (Supplementary Figure 1B).

We calculate the west-east gradient predicted by GIA simulations for each of these ice histories, when paired with the Earth model adopted in the main text, on a 202 km segment between (40°N, 73.2°W) and (40°N, 75.6°W). In the case of modified ICE-5G the gradient is 1.8 mm km^{-1} ky^{-1}. For ICE-PC, ICE-PC2, ICE-PC3, and ICE-PC4, the gradients are 2.5 mm km^{-1} ky^{-1}, 2.0 mm km^{-1} ky^{-1}, 3.0 mm km^{-1} ky^{-1}, and 0.2 mm km^{-1} ky^{-1}, respectively.
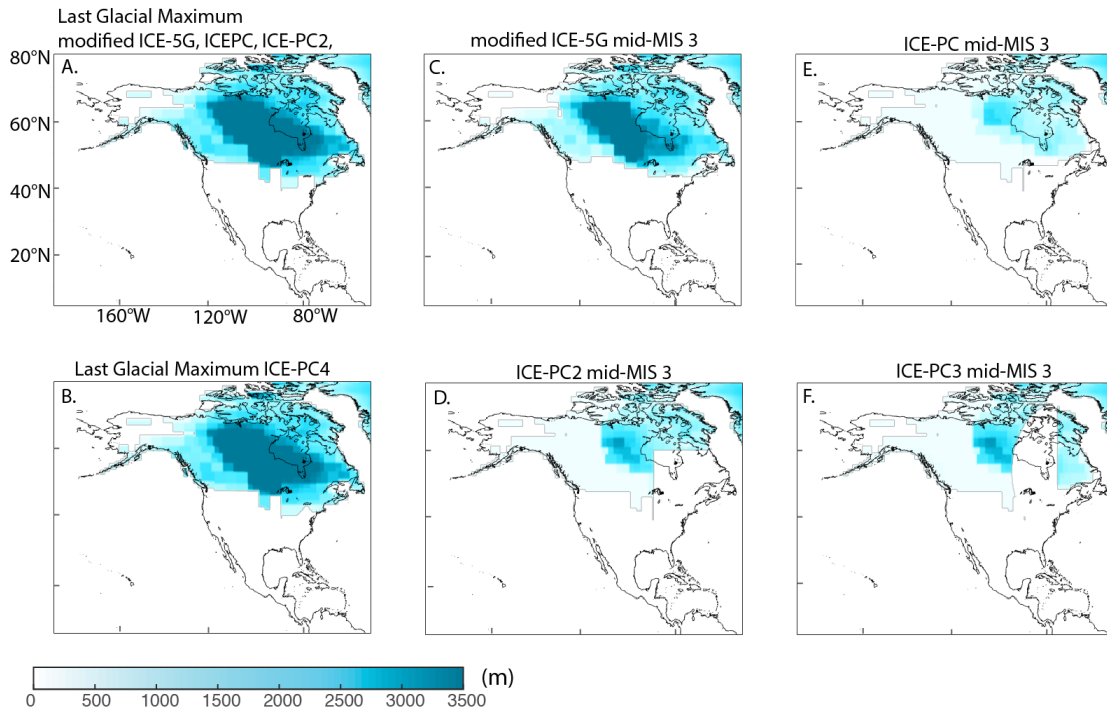
Supplementary Figure 1| A. Ice thickness at the Last Glacial Maximum (26 ka) for the modified ICE-5G, ICE-PC, ICE-PC2, ICE-PC3 histories, B. Ice thickness at the Last Glacial Maximum for ICE-PC4. C-F. Ice thickness at mid-MIS 3 (44 ka) for the modified ICE-5G (C), ICE-PC2 (and ICE-PC4) (D), ICE-PC (E), ICE-PC3 (F) histories.

Supplementary Note 2: Time-variable uplift

In Supplementary Figure 2, vertical displacement rates are plotted at 1 kyr time intervals from 32-26 ka. These fields are input to the CHILD landscape evolution model. The pattern of vertical displacement, especially the amplitude of the west-east gradient, varies substantially over this time period. Inspection of these time frames reveals that the vertical displacement field across the time step 28-27 ka is likely the largest control on the number of eastward diversions noted at the final time step 26 ka. Here, as elsewhere, we use the term "diversion" as a synonym for "avulsion", indicating a shift in a river's course without implications for the cause of the shift.
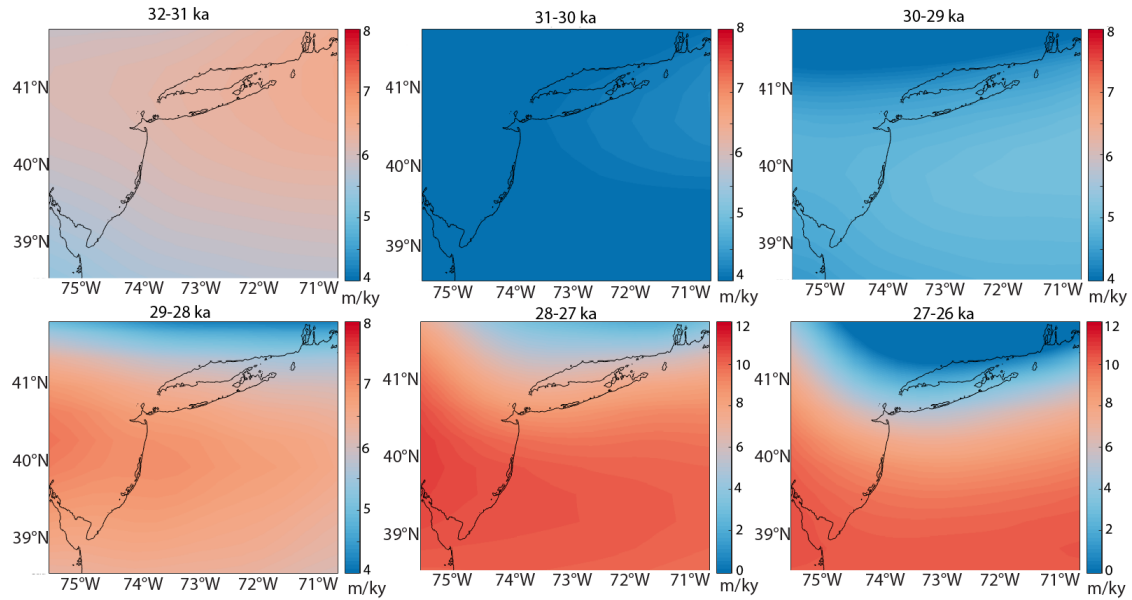
Supplementary Figure 2 | Vertical displacement rates computed using ICE-PC2 from 32-26 ka at 1 ky time intervals. Note the differences in color scales among panels.
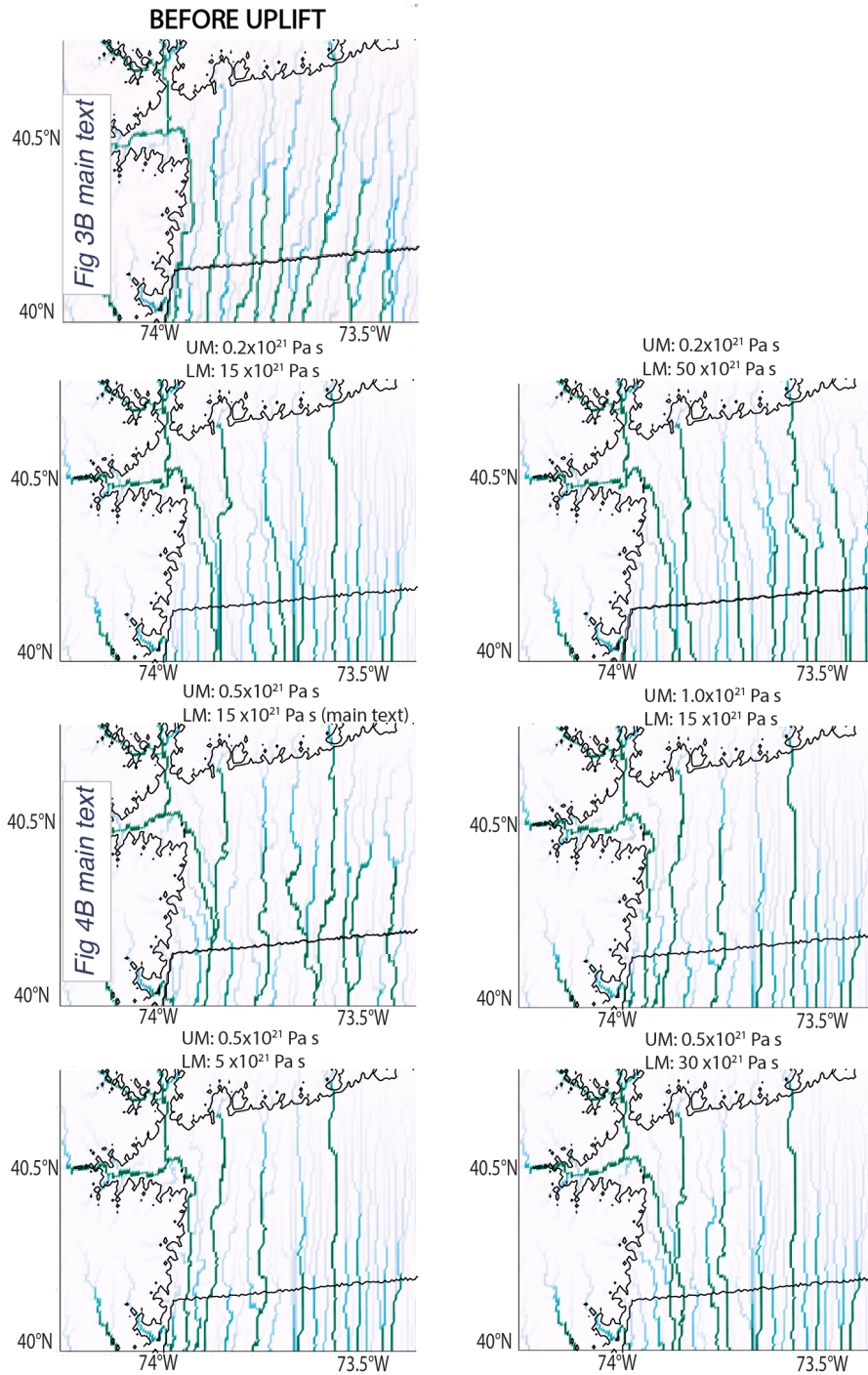
Supplementary Note 3: Sensitivity to mantle viscosity

We assess the sensitivity of our results to Earth structure by varying the upper and lower mantle viscosities in the ranges of $(0.2\text{-}1.0) \times 10^{21}$ Pa s and $(5\text{-}30) \times 10^{21}$ Pa s, respectively. Each of these simulations was driven with the erodibility parameters adopted in the main text (Supplementary Note 5) and ice model ICE-PC2. The number of predicted river diversions is primarily sensitive to the upper mantle viscosity. In particular, the west-east gradient predicted in the GIA calculation increases as one weakens the upper mantle, which leads to more river diversions. Supplementary Figure 3 shows the predicted rate of change in elevation from 32-26 ka for each of these Earth

models, including the Earth model adopted in the main text. Supplementary Figure 4 shows the river channel locations predicted by the landscape evolution simulation at 26 ka.
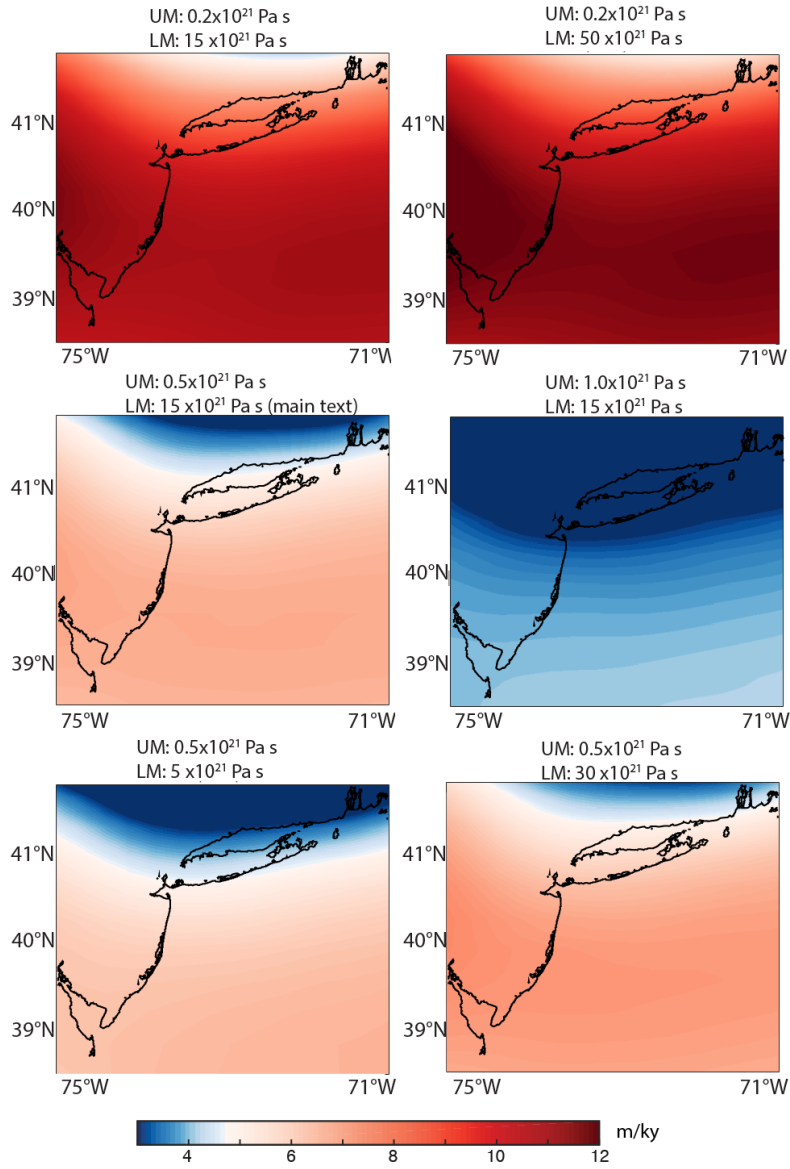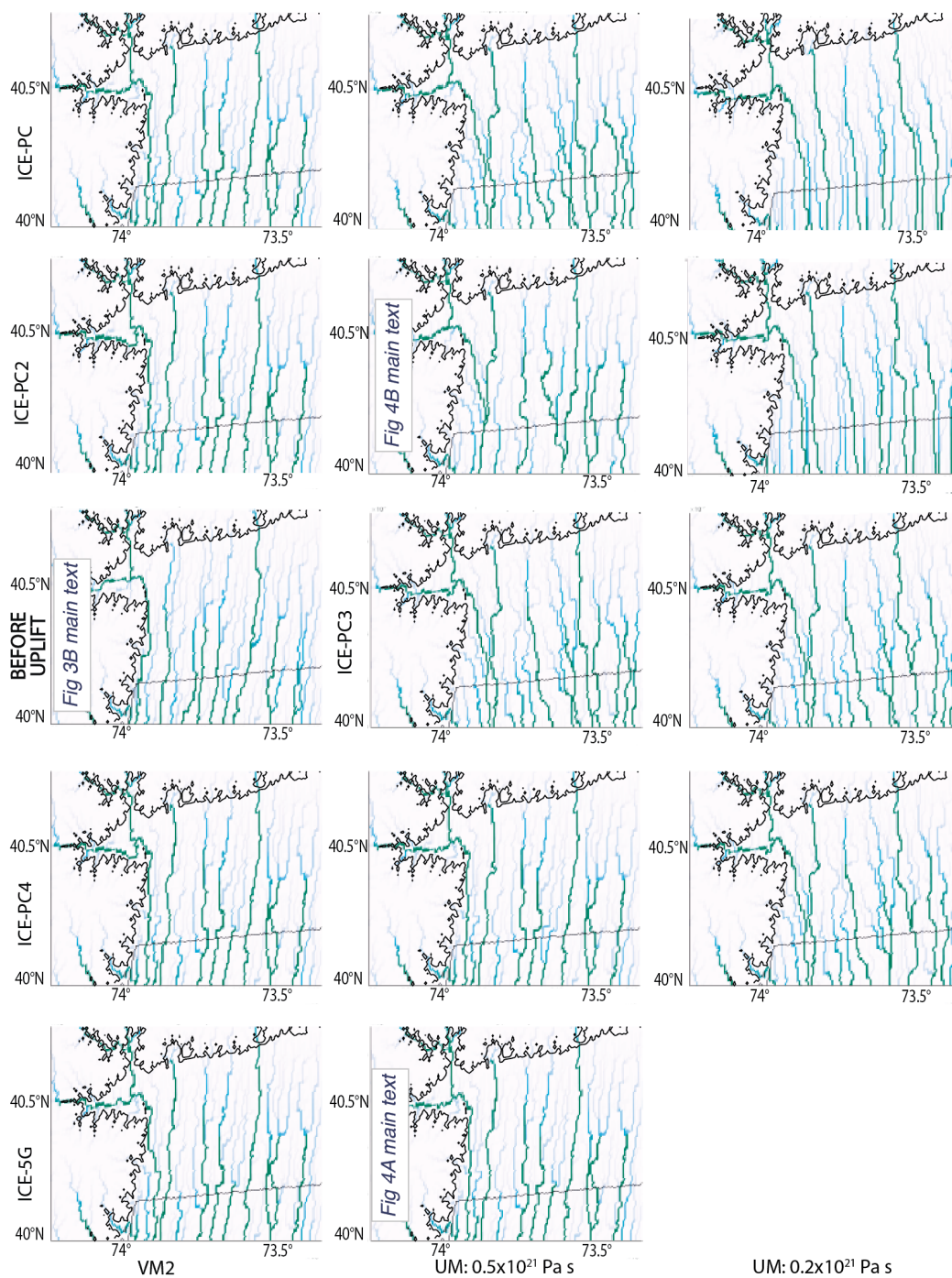

Supplementary Figure 3 | Predicted rate of change in elevation from 32-26 using ice history ICE-PC2 (as in main text) in a GIA simulation paired with a variety of upper (UM) and lower (LM) mantle viscosities.

BEFORE UPLIFT

Fig 3B main text

UM: 0.2x10²¹ Pa s
LM: 15 x10²¹ Pa s

UM: 0.2x10²¹ Pa s
LM: 50 x10²¹ Pa s

UM: 0.5x10²¹ Pa s
LM: 15 x10²¹ Pa s (main text)

Fig 4B main text

UM: 1.0x10²¹ Pa s
LM: 15 x10²¹ Pa s

UM: 0.5x10²¹ Pa s
LM: 5 x10²¹ Pa s

UM: 0.5x10²¹ Pa s
LM: 30 x10²¹ Pa s

Supplementary Figure 4 | Predicted path of rivers using simulations forced by a GIA calculation in which the ice history ICE-PC2 is paired with Earth models sampling a variety of upper (UM) and lower (LM) mantle viscosities (see text). Parameters adopted in the landscape evolution simulation are the same as those adopted in main text. Darker colors are used to highlight relatively larger rivers.
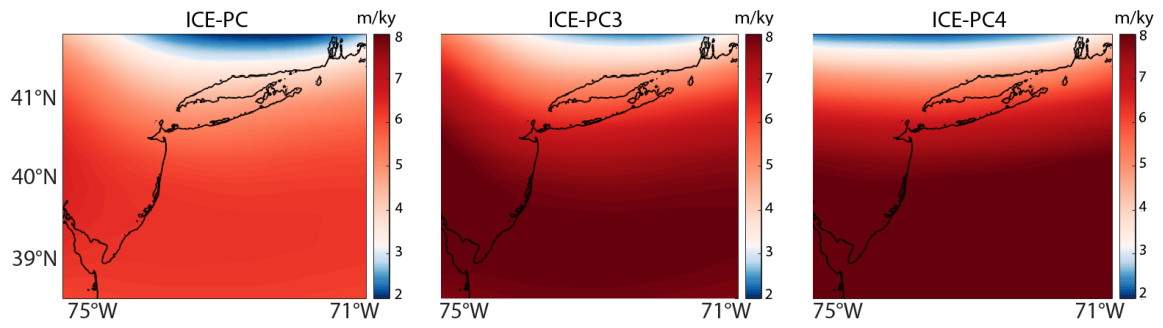
Supplementary Figure 5 | Average rates of vertical displacement (as in Figure 2 of the main text) for ice histories ICE-PC, ICE-PC3, and ICE-PC4.

ICE-PC

ICE-PC2

Fig 4B main text

BEFORE UPLIFT

Fig 3B main text

ICE-PC3

ICE-PC4

ICE-5G

Fig 4A main text

VM2

UM: 0.5x10^{21} Pa s
LM: 15 x10^{21} Pa s
(as in main text)

UM: 0.2x10^{21} Pa s
LM: 50 x10^{21} Pa s

Supplementary Figure 6 | Compilation of landscape evolution simulations for the range of ice models described in Supplementary Note 1 and the range of Earth models described in Supplementary Note 3. Each column represents simulations performed with the Earth model labeled at the bottom of the three columns. Each row represents simulations performed with the ice history labeled at the left. The first column, third row represents the river drainage pattern prior to any imposed crustal deformation.

Supplementary Note 4: Construction of synthetic topography at 32 ka

The initial topography adopted in landscape evolution models can strongly influence predicted erosional and depositional histories. To explore the influence of GIA on river diversions in a generalized landscape, we created a simplified topographic field at 32 ka to represent the initial topography in a region similar to the Hudson shelf, which was subaerial before LGM. Our goal here is not to exactly reproduce the paleotopography on the Hudson shelf, which is not precisely known, but rather to explore the frequency of river diversions in a simplified landscape that captures the most important drivers of diversions: the regional shelf gradient, the initial north-south orientation of the river, and a realistic ice history.

For comparisons of model predictions to field sites like the Hudson Shelf, it is preferable to begin with roughened topography that mimics the irregularity of real topography (Perron & Fagherazzi 2012). In order to create a synthetic map to represent a simplified topography at 32 ka on the Hudson shelf region, we first run a simulation over 100 ky by applying two separate uplift functions to a randomly-generated topography with amplitudes between 0 and 1 m elevation. We outline the present-day continents on this generated topography, and apply one uplift function here and another to the present-day ocean areas (shown in Figure 3A). In continental areas (above present-day sea level)

we apply uplift rates that decrease from north to south from 2 m/ky to 0.5 m/ky. A smaller uplift function is applied to the present-day ocean regions to simulate the lower topographic gradients on the continental shelf (uplift rate gradient decreases from 0.5 m/ky to 0 m/ky from north to south). We simulate bedrock river incision by solving the stream power law, given the uplift rates described above, using the *Fastscape* algorithm over 100 ky, using 1 ky time steps and an erodibility parameter k of $3x10^{-4} m^{-0.8}$ (Braun & Willett 2013) . This method generates topography where elevations are higher toward the north, similar to the actual present-day topography in this region. We ensure that shelf gradients on the reconstructed topography are similar to present-day gradients (1 m/km) by adding an additional tilt with a decreasing north-to-south gradient of 0.03 m/arc-second. Finally, in order to establish a location of the coastline at 32 ka consistent with predicted shorelines on present-day bathymetry (Figure 2C) we uniformly subtract a value of 25 m from the topography established in the last step. The pattern of river drainage on this topographic reconstruction is shown in Figure 3B, where relatively larger rivers (measured by drainage area) are shown in green. In the region depicted in Figure 3B there are 9 large rivers and 10 intermediate rivers. These rivers drain in a general north-south direction, consistent with the paleo-flow direction of the ancestral Hudson River. While this reconstruction yields a simplified version of the regional paleotopography, we believe that the synthetic topography captures the topographic features that are most important in determining whether an eastward diversion occurs, in particular the shelf gradient, the initial north-south orientation of the river, and a realistic ice history.

Supplementary Note 5: Landscape Evolution Model: CHILD

We adopt the landscape evolution model *Channel-Hillslope Integrated Landscape Development* (CHILD) to simulate physical erosion in the synthetic reconstruction of Hudson Shelf topography. This open-source model provides process-based simulations of both bedrock and alluvial rivers, which provide the flexibility to simulate the ancestral Hudson River channel in both detachment-limited and transport-limited fluvial regimes. We drive the landscape evolution simulations by inputting to CHILD an initial topography (Supplementary Note 4) and a time series of vertical displacement fields from 32-26 ka (Supplementary Figure 2). Here we briefly describe our adopted values for key model parameters in CHILD, and refer the reader to the CHILD User Guide for model details (Tucker 2010).

Transport-limited fluvial transport in CHILD is modeled as a function of sediment transport capacity, Q_c, which itself is a function of excess shear stress: $Q_c = K_F W (\tau_0 - \tau_c)^{P_F}$. Here K_F is a transport coefficient, W is channel width, τ_0 is the bed shear stress, τ_c is the critical shear stress, and P_F is a constant scaling exponent. We adopt a value of $\tau_c = 1$ Pa for both bedrock and regolith in our simulations, consistent with field and laboratory measurements implying non-dimensional critical shear stresses τ_c^* of 0.01 to 0.1 (Lamb et al., 2008). For simplicity, we adopt a value of $P_F = 1$, such that the sediment transport capacity is linearly dependent on the shear stress. We note that other sediment transport relations use different values for these parameters (e.g., an exponent of 2.5 on shear stress in Engelund and Hansen, 1967), and that our adopted value of $P_F = 1$ may underestimate the likelihood of GIA-drive avulsion. Future work will explore the sensitivity of GIA-

driven avulsions to alternative sediment transport relations. We adopt a value of $K_F = 5.0$ $m^2 \, yr^{-1} \, Pa^{-1}$.

Bed shear stress is modeled as a function of the water discharge Q and channel gradient S, as in $\tau_0 = K_T(W^{-1}Q)^{M_F}S^{N_F}$, where K_T is a scaling coefficient and M_F and N_F are constant exponents. M_F and N_F are poorly constrained, but the ratio M_F/N_F typically falls between 0.35-0.6 (Whipple & Tucker 1999). We adopt values of $N_F = 1$ and $M_F = 0.4$, consistent with global datasets that show a best fit ratio of ~0.5 (Harel et al., 2016). Lastly, we adopt a value of $K_T = 10^{-6} \, Pa \, (m^2/s)^{-0.4}$, such that we obtain an erosional scaling coefficient (K_FK_T) consistent with values adopted in previous studies (Whipple et al. 2017; Whipple & Tucker 2002).

Detachment-limited fluvial transport in CHILD is modeled as a function of detachment capacity D_c, which itself is a function of excess bed shear stress: $D_c = K_B(\tau_0 - \tau_c)^{P_B}$. Here K_B is a rate coefficient, P_B is a constant exponent, and bed shear stress has the same form as it does in transport-limited conditions: $\tau_0 = K_T(W^{-1}Q)^{M_B}S^{N_B}$. We adopt values of $P_B = 1$ and $K_B = 1$, such that the erosional scaling coefficient is a function of K_TK_F. We adopt the same values for the exponents as the analogous exponents in transport-limited conditions: $N_B = 1$ and $M_B = 0.4$.

Hillslope soil flux q_c is modeled as a nonlinear function of topographic gradient: $q_c = K_D\nabla z[1 - (|\nabla z|/S_c)^2]^{-1}$, where K_D is a soil transport coefficient, z is elevation, and S_c is a critical hillslope gradient. Here we adopt a value of $K_D = 0.01 \, m^2/yr$, consistent with a global compilation of field measurements (Perron 2017), and a value of $S_c = 0.5774$, consistent with values used in example simulations included in the 2011 CHILD release.

Supplementary Table 1. Parameter values adopted in CHILD simulations.

Name	Value	Description
K_B	1 m^2 s/kg	Bedrock erodibility coefficient
K_D	0.01 m^2/yr	Hillslope soil transport coefficient
K_F	5.0 m^2 yr^{-1} Pa^{-1}	Fluvial sediment transport coefficient
K_R	0.0005 m yr^{-1} Pa^{-1}	Regolith erodibility coefficient
K_T	10^{-6} Pa (m^2/s)$^{-0.4}$	Bed shear stress coefficient
M_B	0.4	Discharge exponent in detachment capacity equation
M_F	0.4	Discharge exponent in transport capacity equation
N_B	1	Slope exponent in detachment capacity equation
N_F	1	Slope exponent in transport capacity equation
P_B	1	Excess shear stress exponent in detachment capacity equation
P_F	1	Excess shear stress exponent in transport capacity equation
S_c	0.5774	Threshold gradient for nonlinear creep
τ_c	1 Pa	Detachment threshold for bedrock and regolith

By restricting our simulations to fluvial and hillslope processes, our simulations neglect coastal processes such as backwater effects and delta deposition.

Supplementary Note 6: Sensitivity to erodibility parameters

We ran several simulations to assess the sensitivity of our results to the erodibility parameters adopted in CHILD. In particular, we ran simulations using the ice history ICE-PC2, paired with the Earth model adopted in the main text, and varied τ_c and K_F. For both K_F and τ_c we varied values by two orders of magnitude: K_F from 0.5 to 50 (the value adopted in main text is 5) and τ_c from 0.1 to 10 (the value adopted in main text is 1). When driven by the same GIA-induced deformation field as in main text, these simulations produced the same number of river diversions as in Figure 3B. Thus these simulations suggest that the number of modeled river diversions is primarily sensitive to changes in the imposed field of GIA-induced deformation, rather than to the assumed values of K_F and τ_c within the above ranges.

We also performed simulations adopting the detachment-only option in CHILD to assess the influence of transport-limited conditions on the modeled river diversions. We found that simulations ignoring alluvial processes resulted in predicted river drainage patterns identical to that shown in the main text for both ICE-PC2 and ICE-5G. Thus these simulations suggest that the modeled predictions of river evolution are largely sensitive to changes in slope, which in our simulations is primarily determined by GIA-induced crustal deformation. This may be a consequence of the slope-dependence of both transport-limited and detachment-limited processes, such that GIA-induced changes in slope strongly affect both transport-limited and detachment-limited conditions.

Supplementary Note 7: Results of landscape evolution simulation over an extended time interval

Although the focus of this study is on the diversion of the ancestral Hudson River at ~30 ka, we also explore the evolution of the Hudson River forced by GIA simulations over a longer time interval. Specifically, we ran the simulation for an additional 8 ky, to 18 ka. While rates of vertical displacement from 26-18 ka are much smaller than those over the 32-26 ka interval, a west-east gradient persists, and 4 more rivers are diverted eastward by 18 ka (Supplementary Figure 7).

Because the present-day submarine channel is deeply incised, and this incision is thought to be coincident with the catastrophic drainage of pro-glacial Lake Iroquois, the Hudson River must have been at this position at the time of flooding ~13 ka (Rayburn et al. 2005). Thus, simulations of river evolution forced with GIA vertical displacement histories must predict a river that is east of the ancestral channel at this time. By running

our simulations until 18 ka we note that more eastward diversions are predicted, and rates of crustal deformation decrease sharply after this time. Future studies aimed at continuing simulations through the entire deglaciation phase should include realistic changes in the depositional regime of the river channel. In particular, as base level fell, the Hudson River may have shifted from a depositional to an incisional environment, explaining the entrenchment in the channel after it was diverted eastward.
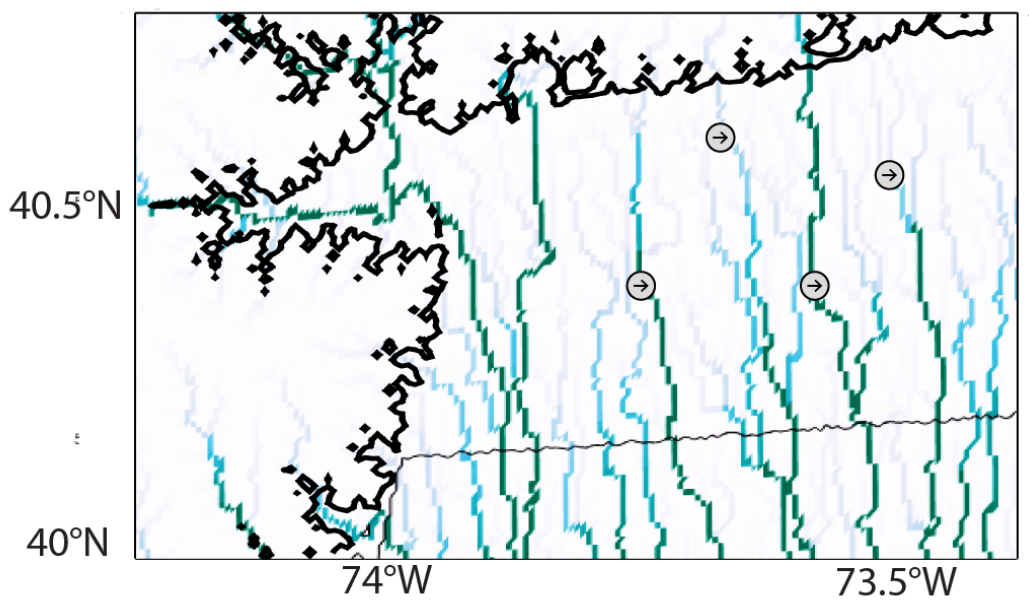
Supplementary Figure 7 | Landscape evolution simulation with ICE-PC2 (as in main text) at 18 ka. River channels are colored in green and blue as in Supplementary Figure 2. Additional diversions that occurred after 26 ka are highlighted in gray circles.

SUPPLEMENTARY REFERENCES

Braun, J. & Willett, S.D., 2013. A very efficient O(n), implicit and parallel method to solve the stream power equation governing fluvial incision and landscape evolution. *Geomorphology*, 180–181, pp.170–179.

Engelund, F., & Hansen, E. (1967). A monograph on sediment transport in alluvial streams. *Technical University of Denmark 0stervoldgade 10, Copenhagen K.*

Harel, M., Mudd, S.M. & Attal, M., 2016. Global analysis of the stream power law parameters based on worldwide Be denudation rates. *Geomorphology*, 268, pp.184–196.

Lamb, M.P., Dietrich, W.E. & Venditti, J.G., 2008. Is the critical shields stress for incipient sediment motion dependent on channel-bed slope? *Journal of Geophysical Research: Earth Surface*, 113(2), pp.1–20.

Löfverström, M., Caballero, R., Nilsson, J., & Kleman, J. (2014). Evolution of the large-scale atmospheric circulation in response to changing ice sheets over the last glacial cycle. *Climate of the Past*, *10*, 1453–1471. http://doi.org/10.5194/cp-10-1453-2014

Perron, J.T., 2017. Climate and the Pace of Erosional Landscape Evolution. *Annual Review of Earth and Planetary Sciences*, 45(1), p.annurev-earth-060614-105405.

Perron, J.T. & Fagherazzi, S., 2012. The legacy of initial conditions in landscape evolution. *Earth Surface Processes and Landforms*, 63(August 2011), pp.52–63.

Rayburn, J.A., Knuepfer, P.L.K. & Franzi, D.A., 2005. A series of large , Late Wisconsinan meltwater floods through the Champlain and Hudson Valleys , New York State , USA. *Quat. Sci. Reviews*, 24, pp.2410–2419.

Tucker, G.E., 2010. CHILD users guide for version R9.4.1. http://csdms.colorado.edu/mediawiki/images/Child_users_guide.pdf.

Whipple, K. X., Forte, A. M., DiBiase, R. A., Gasparini, N. M., & Ouimet, W. B. (2017). Timescales of landscape response to divide migration and drainage capture: Implications for the role of divide mobility in landscape evolution. *Journal of Geophysical Research: Earth Surface*, *122*(1), 248–273. http://doi.org/10.1002/2016JF003973

Whipple, K.X. & Tucker, G.E., 1999. Dynamics of stream-power river incision model. *Journal of Geophysical Research*, 104(August), pp.661–674.

Whipple, K.X. & Tucker, G.E., 2002. Implications of sediment-flux-dependent river incision models for landscape evolution. *Journal of Geophysical Research*, 107.